ACS NANO

www.acsnano.org

Article

Fast and Trap-Minimized Li Transport via Size-Mismatch-Driven Cation-Ordering Control in Li-Excess Disordered Rocksalt Cathodes

Jinho Ahn,[¶] Bonyoung Ku,[¶] Hyunji Kweon, Hoseok Lee, Hobin Ahn, Myungeun Choi, Myeong Hwan Lee, Moonsu Yoon, Junghyun Choi, Jihyun Hong,* and Jongsoon Kim*

Cite This: *ACS Nano* 2026, 20, 10556−10569

Read Online

ACCESS | Metrics & More | Article Recommendations | Supporting Information

ABSTRACT: Li-excess cation-disordered rocksalt (DRX) is considered a promising cathode for lithium-ion batteries owing to its high-energy densities. However, short-range cation ordering (SRCO) commonly arises in DRX cathodes due to local electrostatic interactions and size similarities among cations, resulting in Li-trapping and sluggish Li-transport. Here, we propose that the SRCO suppression in the DRX system can be achieved without complex high-entropy composition by simultaneously tuning electrostatic interactions and the cationic size effect. The incorporation of Ti^{4+} into Li−Nb/Mn DRX, being lower-valent and smaller than Nb^{5+}, weakens high-valence-driven interactions and increases the ionic size mismatch with Li^+, thereby promoting Li/TM mixing and energetically disfavoring the SRCO formation. Thus, a low-entropy DRX, $Li_{1.2}Nb_{0.15}Mn_{0.55}Ti_{0.1}O_2$ (LNM-0.1Ti) exhibits significantly enhanced Li^+ transport, reduced voltage hysteresis, and improved structural stability compared to $Li_{1.2}Nb_{0.2}Mn_{0.6}O_2$ (LNM) due to disruption of SRCO. LNM-0.1Ti delivers a high capacity of ∼327 mAh g^{-1} and an energy density of ∼1026 Wh kg^{-1}, outperforming LNM (∼274 mAh g^{-1}, ∼837 Wh kg^{-1}). Notably, the higher-Ti composition, $Li_{1.2}Nb_{0.1}Mn_{0.5}Ti_{0.2}O_2$, exhibits reduced rate capability and energy density compared with LNM-0.1Ti, underscoring the importance of compositional balance in optimizing low-entropy DRX performance. These findings highlight a practical strategy for the development of high-performance DRX cathodes.

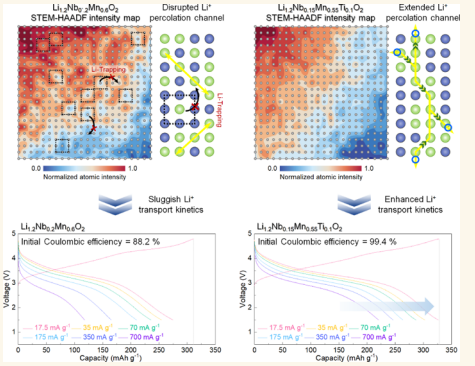

KEYWORDS: *cation-disordered rocksalt cathodes, low-entropy, cation-ordering, electrostatic interactions, size-mismatch*

As global warming continues to raise environmental concerns, the need for renewable energy sources and efficient methods of energy storage and use has become increasingly important.[1−4] Lithium-ion batteries (LIBs) have become the dominant energy storage technology for portable electronics and electric vehicles, due to their high energy density, superior power capability, and long cycle life.[5−9] Enhancing the energy density of cathode materials is essential and is a key requirement for next-generation LIBs.[10,11] One promising strategy is to exploit both cationic transition-metal (TM) redox and anionic oxygen redox reactions in Li-excess cathode materials with the general formula of $Li_{1+x}[TM]_{1-x}O_2$. Among them, Li-rich layered oxides can deliver a specific capacity exceeding 250 mAh g^{-1} through oxygen redox reactions associated with Li−O−Li local configurations.[12−14] These configurations induce labile oxygen states located above the TM 3d orbitals.[15,16] However, despite their high energy density, these materials suffer from structural degradation during cycling—such as TM migration into Li layers and irreversible oxygen loss—caused by the thermodynamic instability of oxidized oxygen species, ultimately leading to poor electrochemical performance.[17−19]

Recently, Li-excess cation-disordered rocksalt (DRX) has emerged as promising cathode materials for high-energy LIBs.[20−22] In DRX structures, TMs and Li ions occupy the same crystallographic sites, resulting in a homogeneous cation-disordered framework. This configuration imparts high structural stability, suppressing structural deformation and O_2 gas evolution even during prolonged cycling—unlike Li-rich layered oxides.[20,23] DRX materials do not require long-range layered ordering, offering broad compositional flexibility such as the use of Co/Ni-free and earth-abundant chemistries while maintaining a rocksalt-derived framework. In addition, because the cation sublattice is already disordered, DRX cathodes can be less sensitive to additional cation rearrangement during cycling.[20,24] However, the lack of long-range cationic ordering hinders the formation of continuous Li^+ transport pathways, thereby limiting the rate capability and practical viability of DRX cathodes. Efficient Li^+ transport in DRX materials relies on the presence and connectivity of numerous 0-TM percolating networks, in which Li^+ migrates through tetrahedral sites that do not share faces with TM-centered octahedra.[25,26] Moreover, the

Received: December 17, 2025
Revised: March 13, 2026
Accepted: March 13, 2026
Published: March 24, 2026

https://doi.org/10.1021/acsnano.5c22044
ACS Nano 2026, 20, 10556−10569

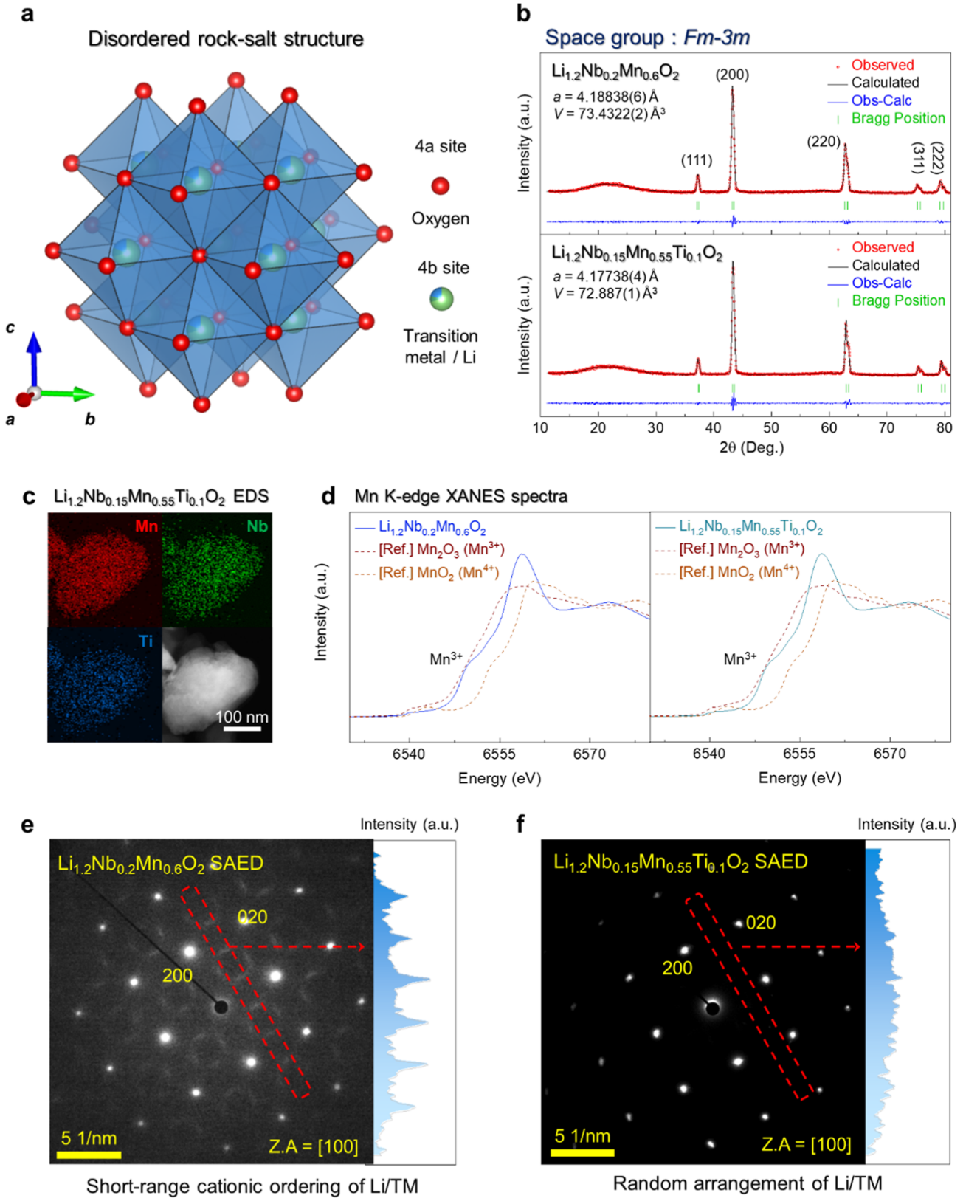

Figure 1. (a) Crystal structure of Li-excess DRX cathode material. (b) XRD patterns and Rietveld refinement results of bare LNM (R_p = 5.70%, R_I = 7.21%, R_F = 1.07%, and χ^2 = 1.34%) and bare LNM-0.1Ti (R_p = 9.58%, R_I = 7.04%, R_F = 1.56%, and χ^2 = 1.58%). (c) TEM-EDS elemental mapping of LNM-0.1Ti (atomic ratio of Nb:Mn:Ti = ~0.15:~0.55:~0.10). (d) Mn K-edge XANES spectra of pristine LNM and LNM-0.1Ti. SAED patterns along the [100] zone axis for (e) LNM and (f) LNM-0.1Ti. The diffuse scattering intensity highlighted with red dots in the SAED pattern is shown on the right.

https://doi.org/10.1021/acsnano.5c22044
ACS Nano 2026, 20, 10556−10569

redox activity is dominated by the Mn^{3+}/Mn^{4+} couple, but the presence of Jahn–Teller active Mn^{3+} can induce anisotropic distortion of MnO_6 octahedra, introducing local strain and disrupting Li-percolation networks.[27] Therefore, precise control over local atomic arrangements is critical to improving the electrochemical reaction kinetics and stability.

RESULTS AND DISCUSSION

SRCO Suppression Strategy

The recent studies have revealed that the presence of $[Li_3Fe_3]$-like short-range cationic ordering (SRCO) within the DRX structure causes Li ions to become trapped by surrounding TMs, thereby reducing the connectivity of Li^+ transport pathways and leading to limited power capability.[28−30] Although high-entropy strategies involving four or more cation species and multiple anion types have been proposed to suppress SRCO, these systems can face difficulties in achieving compositional uniformity at the particle level and often involve complex synthetic processes.

In conventional Li–Nb/Mn DRX systems, SRCO originates from a strong local preference for charge neutrality between high-valence Nb^{5+} (d_0) and Li^+ cations.[31] The resulting SRCO is further modulated by a moderate ionic size mismatch (Nb^{5+}: 0.64 Å, Mn^{3+}: 0.65 Å, Li^+: 0.76 Å), while Jahn–Teller distortion of Mn^{3+} induces spatial strain that can reinforce specific site preferences of certain cations. Accordingly, we hypothesized that simultaneous control of electrostatic interactions (charge effect) and cationic size effect would enable disruption of SRCO even in low-entropy compositions, without relying on multi-cation high-entropy designs. This interpretation is consistent with prior reports that SRCO in Li-excess DRX is governed by the coupled roles of charge effects and ionic-size mismatch, which together balance local ordering versus cation mixing; tuning these factors can promote more homogeneous Li/TM mixing, reduce local strain, and destabilize SRCO.[31,32] The incorporation of Ti^{4+} (0.61 Å), which has a smaller ionic radius and lower charge than Nb^{5+}, selectively rebalances these contributions: (i) it reduces the fraction of high-valence Nb^{5+} and thus weakens the electrostatic driving force, and (ii) it increases the size mismatch with Li^+, facilitating Li/TM mixing to relieve local strain. This mixing can destabilize the formation of ordered cation arrangements, making the suppression of SRCO energetically favorable, even in a low-entropy DRX system. The coupled roles of the charge effect and cation-size mismatch in destabilizing SRCO are schematically summarized in Figure S1 (Supporting Information).

In this work, transmission electron microscopy (TEM) analysis clearly revealed that the low-entropy DRX composition $Li_{1.2}Nb_{0.15}Mn_{0.55}Ti_{0.1}O_2$ (LNM-0.1Ti) exhibited disrupted SRCO, in contrast to its conventional counterpart $Li_{1.2}Nb_{0.2}Mn_{0.6}O_2$ (LNM). Especially, intensity mapping analysis based on scanning transmission electron microscopy high-angle annular dark-field (STEM-HAADF) data directly confirmed minimized Li-trapping and extended Li-transport pathways in LNM-0.1Ti, which contribute to enhanced power capability.

At a current density of 17.5 mA g^{-1}, LNM-0.1Ti delivers a high reversible capacity of ∼327 mAh g^{-1} and an energy density of ∼1026 Wh kg^{-1}, outperforming LNM (∼274 mAh g^{-1}, ∼837 Wh kg^{-1}). Notably, the performance gap widens at high current densities. Even at 700 mA g^{-1}, LNM-0.1Ti maintains ∼220 mAh g^{-1} and ∼606 Wh kg^{-1}, whereas LNM exhibits ∼118 mAh g^{-1} and ∼301 Wh kg^{-1}. LNM-0.1Ti also retains ∼71% of its initial capacity after 100 cycles compared to ∼51% for LNM, highlighting the importance of SRCO disruption in achieving long-term cycling stability. Particularly, increasing the Ti content to 0.2 mol in $Li_{1.2}Nb_{0.2}Mn_{0.5}Ti_{0.2}O_2$ (LNM-0.2Ti) leads to a noticeable decrease in rate capability and energy density, underscoring the importance of maintaining compositional balance for enhanced electrochemical performance in low-entropy DRX cathodes. *Operando* X-ray diffraction (XRD) and first-principles calculations consistently showed that LNM-0.1Ti undergoes more stable structural evolution during charge–discharge compared to LNM. This enhanced structural reversibility is attributed to the suppression of SRCO, which in turn supports improved electrochemical performance.

To prepare LNM-0.1Ti and LNM, we used a conventional solid-state synthesis method. To enhance the electrical conductivity, the powders were ball-milled with conductive carbon. Detailed synthesis procedures are provided in the Experimental Section. As shown in Figure 1a, the low-entropy composition LNM-0.1Ti adopts a typical Li-excess DRX-type crystal structure, in which TM ions randomly occupy the 4a lattice sites and oxygen ions exclusively occupy the 4b sites. XRD patterns (Figure 1b) confirm that both LNM-0.1Ti and LNM have identical long-range atomic arrangements (cubic $Fm\bar{3}m$, space group number 225), with negligible impurity phases. In addition, the broad feature around $2\theta \approx 20°$ can be interpreted as a low-angle diffuse scattering component commonly observed in DRX materials, rather than a diffraction peak from a separate crystalline impurity phase.[20,33,34] Rietveld refinement reveals that LNM-0.1Ti has a slightly smaller lattice parameter (a = 4.17738(4) Å) compared to LNM (a = 4.18838(6) Å), indicating successful incorporation of Ti ions into the crystal lattice forming a solid-solution phase (Tables S1 and S2, Supporting Information). The refinement quality is supported by low R-factors (R_p = 9.58%, R_I = 7.04%, R_F = 1.56%, and χ^2 = 1.58%). The similarity in peak intensity and full width at half-maximum (fwhm) between LNM and LNM-0.1Ti (Figure S2, Supporting Information) suggests comparable crystallite sizes and microstrain. SEM analysis further verifies that LNM-0.1Ti and LNM exhibit similar particle morphology and size distributions (Figure S3, Supporting Information).

TEM equipped with EDS elemental mapping (Figure 1c) reveals homogeneous distributions of Nb, Mn, and Ti within LNM-0.1Ti particles (∼500 nm in diameter). Elemental ratios from TEM-EDS (Nb:Mn:Ti = ∼0.15:0.55:0.1) are consistent with ICP-AES results (Table S3, Supporting Information). Synchrotron-based X-ray absorption near-edge structure (XANES) analysis confirms the predominance of Mn^{3+} ions in both LNM-0.1Ti and LNM (Figure 1d), indicating that the Mn^{3+}/Mn^{4+} redox reaction can occur in both cathodes. The oxidation states of Nb^{5+} and Ti^{4+} in LNM-0.1Ti are also verified by XANES (Figure S4, Supporting Information).

While both materials exhibit similar long-range structures, SAED analysis reveals distinct differences in local ordering over a broader spatial region. The SAED pattern of LNM (Figure 1e) displays ring-like diffuse scattering superimposed on the primary rocksalt reflections of the (200) and (020) planes along the [100] zone axis, as highlighted with the intensity histogram in the right panel. These diffuse scattering features are indicative of SRCO between Li and TM ions, consistent with previous reports on Li-excess DRX materials.[31,35] In contrast, the low-entropy LNM-0.1Ti exhibits a well-defined, single-crystal-like diffraction pattern without ring features (Figure 1f) suggesting

https://doi.org/10.1021/acsnano.5c22044
ACS Nano 2026, 20, 10556−10569

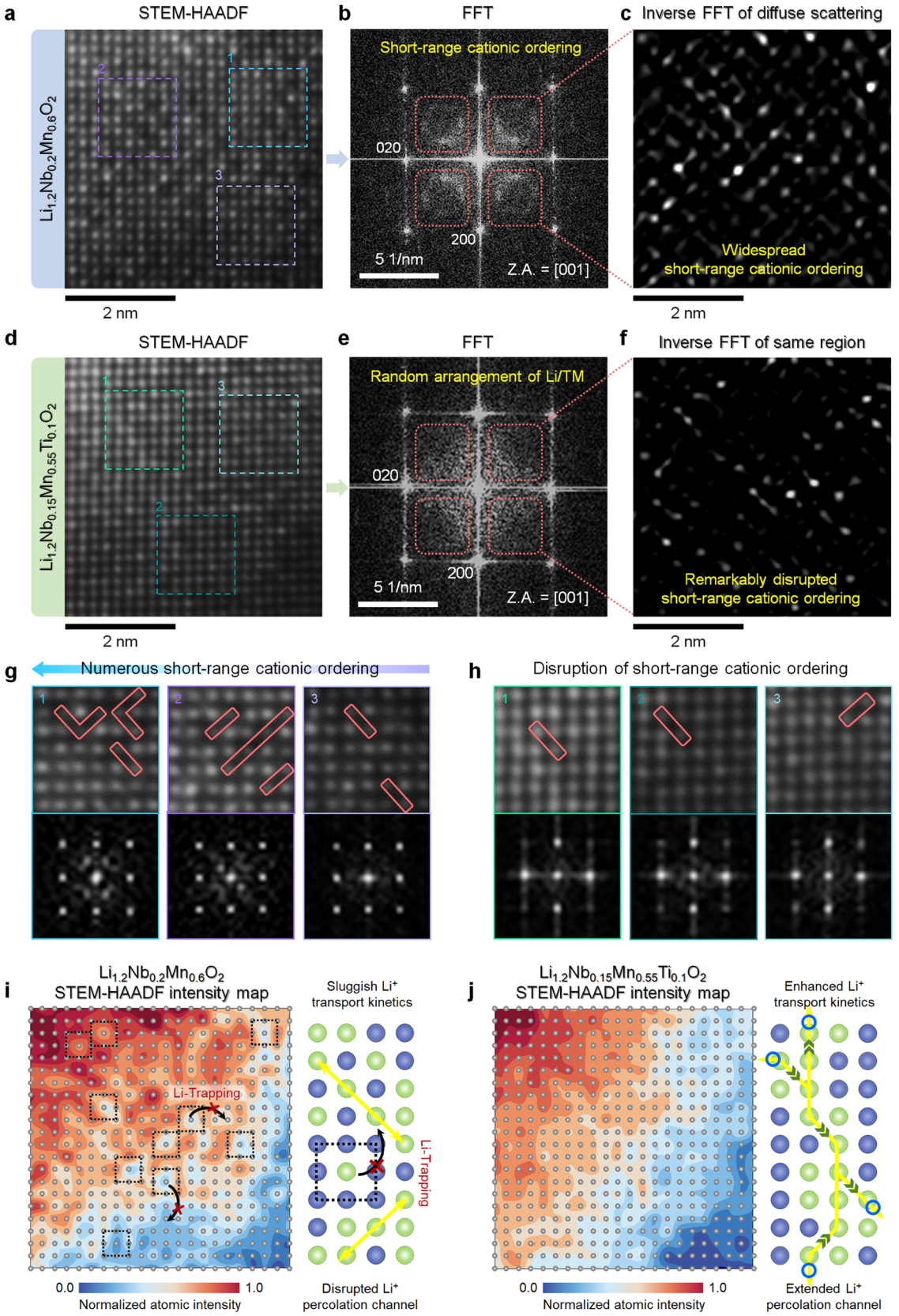

Figure 2. (a–c) STEM-HAADF image of LNM, the corresponding FFT pattern along the [001] zone axis, and inverse FFT image masked with diffuse scattering regions associated with SRCO. (d–f) STEM-HAADF image of LNM-0.1Ti, the corresponding FFT pattern along the [001] zone axis, and inverse FFT image masked using the same regions as in (c). (g,h) Magnified STEM-HAADF images and FFT patterns for the selected areas in LNM and LNM-0.1Ti, respectively (indicated as region 1 to 3; each square area includes 7 × 7 atoms). (i,j) Intensity color mapping based on STEM-HAADF images of LNM and LNM-0.1Ti, respectively. A schematic diagram illustrating the influence of SRCO on Li^+ transport is shown on the right.

https://doi.org/10.1021/acsnano.5c22044
ACS Nano 2026, 20, 10556–10569

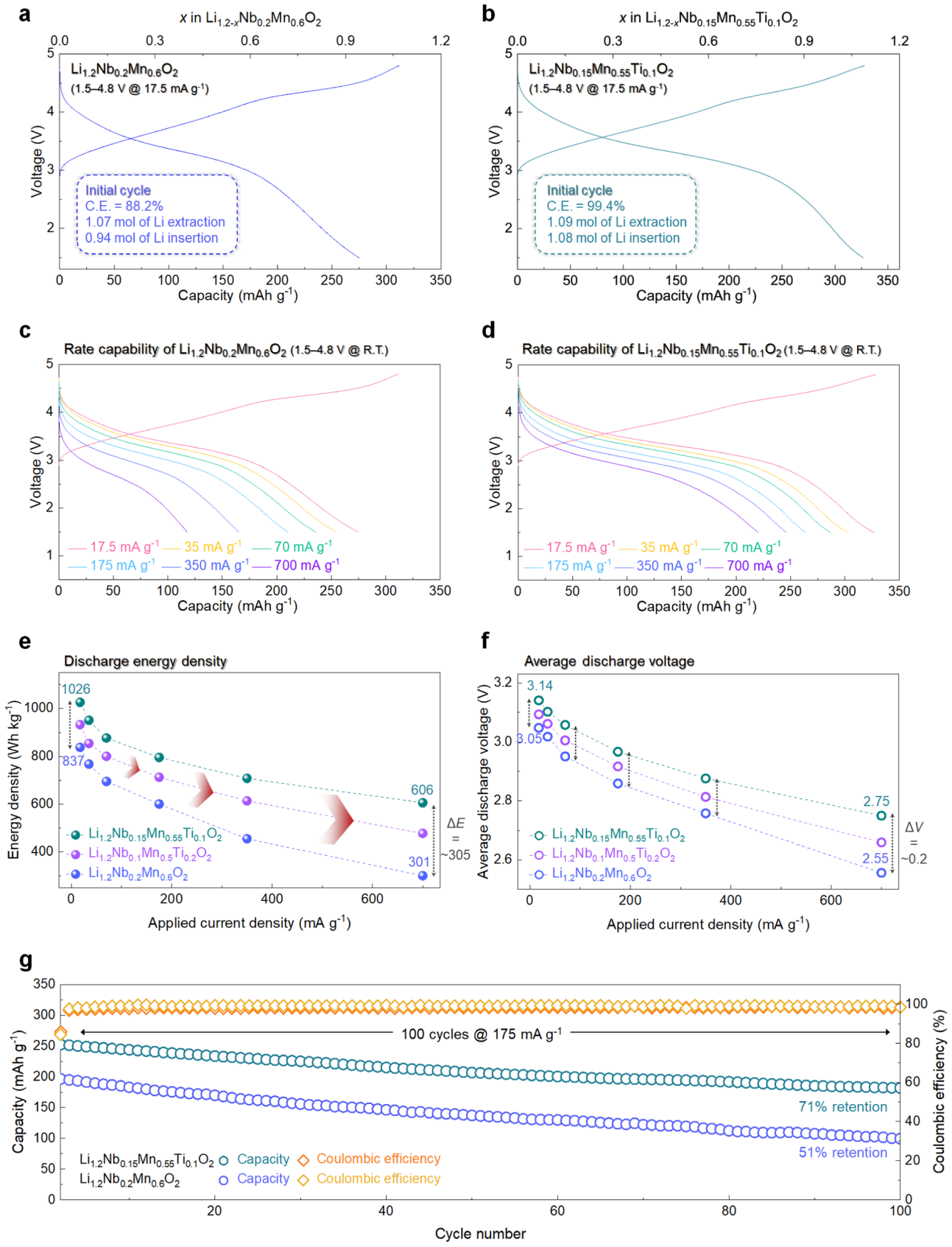

Figure 3. First charge/discharge curves of (a) LNM and (b) LNM-0.1Ti in the voltage range of 1.5−4.8 V (vs Li^+/Li) at a current density of 17.5 mA g^{-1}. Charge/discharge curves of (c) LNM and (d) LNM-0.1Ti in the voltage range of 1.5−4.8 V at various discharge current densities with a fixed charge current density of 17.5 mA g^{-1}. Comparison of (e) energy density and (f) average discharge voltage between LNM, LNM-0.1Ti, and LNM-0.2Ti at various current densities. (g) Cycling performance of LNM and LNM-0.1Ti over 100 cycles at 175 mA g^{-1}.

https://doi.org/10.1021/acsnano.5c22044
ACS Nano 2026, 20, 10556−10569

that 0.1 mol of Ti-substitution into LNM-0.1Ti effectively disrupts SRCO and induces a more randomized cationic distribution. The observed disruption of SRCO, as expected, became achievable in low-entropy compositions by simultaneously modulating the charge effect and cationic size effect.[31] The incorporation of Ti^{4+} (0.61 Å), which has a smaller ionic radius and lower charge than Nb^{5+}, promotes Li/TM mixing to alleviate electrostatic interactions and local lattice strain, thereby rendering SRCO formation energetically unfavorable.

Atomic-Scale SRCO Suppression and Li Percolation

To investigate the local atomic ordering and confirm the disruption of SRCO in LNM-0.1Ti, we conducted STEM-HAADF analysis as a high-resolution local visualization complementary to the SAED results. As shown in Figure 2a, LNM exhibits a cubic crystal structure typical of Li-excess DRX cathodes. In this STEM-HAADF analysis, the TM intensity refers to the relative column brightness and is not element-resolved among Nb, Mn, and Ti. Because the STEM-HAADF intensity is affected not only by atomic number but also by projection along the viewing direction, specimen thickness, and zone-axis alignment, it cannot quantitatively separate the contributions of different TM species in this system. Accordingly, the intensity contrast is used to distinguish TM-rich versus Li-rich columns and to discuss the spatial distribution of local motifs relevant to Li percolation rather than to quantify local enrichment of a specific TM element. Fast Fourier transform (FFT) analysis of the corresponding region (Figure 2b) reveals diffuse scattering features, consistent with the SAED result and indicative of SRCO. This SRCO resembles the $[Li_3Fe_3]$ superlattice structure observed in cubic $LiFeO_2$[35−37] where Li^+ and Fe^{3+} ions alternate in a 3:3 ratio within six octahedral sites (Figure S5, Supporting Information). Inverse FFT analysis of the diffuse scattering patterns further confirms the widespread presence of such locally ordered domains in the LNM (Figure 2c).

In contrast, the STEM-HAADF image of LNM-0.1Ti—a DRX composition with deliberately low configurational entropy—shows no evidence of SRCO (Figure 2d). FFT and inverse FFT analyses (Figure 2e,f) reveal a more homogeneous diffraction pattern without characteristic diffuse scattering. Magnified views of selected regions (Figure 2g,h) highlight the presence of diagonally aligned, low-intensity atomic columns—characteristic of Li-rich configurations—in LNM, while such features are rarely observed in LNM-0.1Ti, supporting the notion that limiting the diversity of TM species and maintaining a Mn-dominant composition can suppress local cation ordering. This observation is consistent with the hypothesis that a low configurational entropy mitigates SRCO by reducing the probability of specific cation−cation preferences that drive short-range order.

In DRX structures, Li^+ ions migrate between octahedral sites through intermediate tetrahedral sites, which are coordinated by varying numbers of TM ions, ranging from 4-TM to 0-TM configurations (Figure S6, Supporting Information). Li^+ transport is most favorable through 0-TM and 1-TM environments due to reduced electrostatic repulsion.[28,35,38] In LNM, the $[Li_3Fe_3]$-like SRCO likely forms 3-TM and 2-TM configurations, increasing the transport barrier and thereby increasing the tortuosity of the Li^+ percolating pathways. In contrast, LNM-0.1Ti, owing to its disrupted SRCO and cationic randomness, exhibits a higher fraction of 0-TM and 1-TM configuration environments, facilitating Li^+ transport and enhancing the electrochemical reaction kinetics.

To further visualize the spatial distribution of SRCO in LNM and LNM-0.1Ti, we mapped the STEM-HAADF intensity of the regions in Figure 2a,d. All STEM-HAADF images were acquired under identical conditions from thin regions with careful zone-axis alignment to minimize thickness and orientation effects, and the intensity maps are discussed in terms of relative variations within the same region. The intensity value at each interpolated point was calculated by applying arithmetic averaging of the surrounding atomic intensities, and the resulting continuous midpoints were connected to generate a two-dimensional intensity map, while the corresponding as-collected 22 × 22 maps are provided for reference (LNM in Figure S7 and LNM-0.1Ti in Figure S8, Supporting Information). As shown in Figure 2i, LNM exhibits frequent Li-rich clusters—low-intensity Li columns surrounded by high-intensity TM columns—corresponding to $[Li_3Fe_3]$-like SRCO. These clusters may trap Li^+ ions and obstruct its transport by forming high-TM coordination environments surrounding the possible percolation networks. In contrast, the low-entropy LNM-0.1Ti displays a more spatially randomized and homogeneous distribution of Li and TM atoms, forming a percolation-friendly environment with minimal local trapping (Figure 2j).

Additionally, interatomic distance analysis (Figure S9, Supporting Information) reveals that LNM-0.1Ti exhibits uniform bond lengths (~2.1 Å), while LNM shows locally contracted bonds (~1.7 Å) near Li-rich regions. This result indicates that the Jahn−Teller distortion of Mn^{3+} is significantly suppressed in LNM-0.1Ti, further contributing to its enhanced structural stability and Li^+ mobility.

Enhanced Kinetics and Durability of Low-Entropy LNM-0.1Ti

The electrochemical performance of LNM-0.1Ti, a low-entropy DRX cathode with disrupted SRCO, was evaluated and compared to that of LNM. As shown in Figure 3a,b, LNM-0.1Ti exhibits a specific capacity of ~327 mAh g^{-1} at a current density of 17.5 mA g^{-1} within the voltage range of 1.5−4.8 V (vs Li^+/Li), exceeding that of LNM (~274 mAh g^{-1}). Notably, LNM-0.1Ti exhibits an initial Coulombic efficiency above 99%, while LNM shows an initial Coulombic efficiency of approximately 90%, indicating improved reversibility. This enhancement is attributable to the disruption of SRCO, which facilitates more favorable Li^+ transport kinetics in low-entropy LNM-0.1Ti.

Rate capability measurements made under various current densities (Figures 3c,d and S10, Supporting Information) show that LNM-0.1Ti consistently outperforms LNM. Even at a high current density of 700 mA g^{-1}, LNM-0.1Ti maintains a discharge capacity of ~220 mAh g^{-1}, higher than ~118 mAh g^{-1} for LNM. In addition to higher capacity, LNM-0.1Ti also exhibits greater average discharge voltage and energy density across all rates (Figure 3e,f). At 700 mA g^{-1}, the voltage and energy density gaps between LNM-0.1Ti and LNM reach ~0.2 V and ~305 Wh kg^{-1}, respectively. Notably, further increasing the Ti content to 0.2 mol (LNM-0.2Ti) results in a significant decline in rate performance despite maintaining a similar DRX structure (Figure S11, Supporting Information). This contrast highlights that the superior performance of LNM-0.1Ti arises not merely from Ti incorporation but from precise compositional tuning that balances cation disorder and Li^+ transport. Electrochemical impedance spectroscopy (EIS) further sup-

https://doi.org/10.1021/acsnano.5c22044
ACS Nano 2026, 20, 10556−10569

ports these findings. As shown in Figure S12 in the Supporting Information, the fitted charge transfer resistance (R_{ct}) of LNM-0.1Ti in the pristine state is ~78.8 Ω, significantly lower than that of LNM (~103 Ω). These EIS spectra were measured in Li-metal half cells (two-electrode configuration); thus, the spectra and fitted parameters represent effective cell-level values that can include contributions from the Li metal and electrolyte. Accordingly, the lower R_{ct} is interpreted as a comparative indication of improved overall interfacial and charge-transfer kinetics under identical testing conditions, consistent with its reduced SRCO discussed above. Supporting these kinetic indicators, galvanostatic intermittent titration technique (GITT) measurements show a higher Li^+ diffusivity for LNM-0.1Ti (~4.59×10^{-10} cm^2 s^{-1}) than for LNM (~2.82×10^{-10} cm^2 s^{-1}) (Figure S13, Supporting Information). Because the GITT-derived diffusivity in porous composite electrodes depends on the assumed active area, the geometric electrode area was used for S. Therefore, the reported D_{Li^+} values represent apparent diffusivities intended for a qualitative comparison between samples tested under identical conditions. Further details of the GITT analysis are provided in the Supporting Information. These results underscore the advantage of using a compositionally simplified, low-entropy approach in DRX cathodes to achieve more efficient Li^+ transport and reduced overpotentials at high current densities, thereby improving both the power and energy performance.

To further assess the structural robustness of LNM-0.1Ti, cycling stability tests were performed (Figure 3g). After 100 cycles, LNM-0.1Ti retained approximately 71% of its initial capacity, while LNM retained only ~51%, confirming that SRCO disruption in the low-entropy composition leads to enhanced structural integrity and long-term durability. In some Mn-rich DRX cathodes, the formation of spinel-like domains during cycling has been reported to be associated with an increased capacity contribution in the high-voltage region.[39] However, both LNM and LNM-0.1Ti do not show a clear tendency for such spinel-like plateau components to newly appear or progressively grow as cycling proceeds, as evidenced by their voltage profiles at the first, 10th, 20th, and 50th cycles shown in Figures S14 and S15 in the Supporting Information. These observations indicate that under the present composition and cycling conditions, the electrochemical performance enhancement observed for LNM-0.1Ti is not accompanied by signatures of a spinel-like δ-phase transformation. LNM-0.2Ti, with higher Ti content, also exhibited a capacity retention of ~72% under the same conditions, comparable to that of LNM-0.1Ti (Figure S11, Supporting Information). To benchmark its performance, we compared LNM-0.1Ti with other reported oxide-based Li-excess DRX cathodes.[31,40−46] As shown in Figure 4a,b, LNM-0.1Ti exhibits superior rate capability and energy density, demonstrating that compositionally driven SRCO disruption through a low-entropy design is an effective strategy for improving both the structural and electrochemical performance in DRX systems.

Suppressed Phase Separation Enables Reversible Oxygen Redox

Using *operando* XRD analysis, we compared the structural evolutions of LNM and LNM-0.1Ti during electrochemical cycling. As shown in Figure 5a, the LNM undergoes an irreversible phase transition during the initial charge. The (200) diffraction peak near 43° shifts to higher angles due to lattice contraction upon Li^+ extraction. Notably, peak splitting

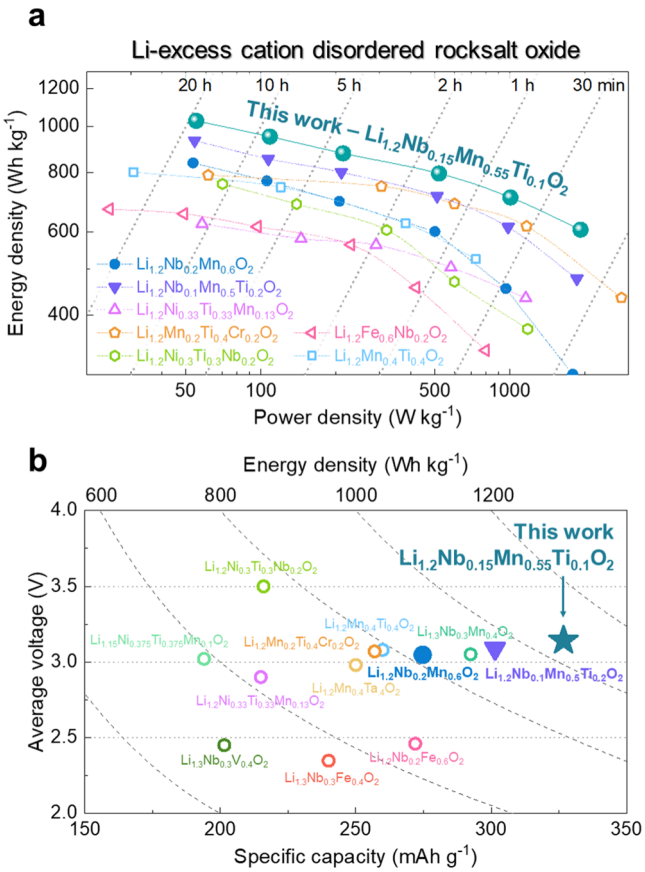

Figure 4. (a) Ragone plot comparing LNM-0.1Ti with previously reported Li-excess DRX cathode materials. (b) Comparison of the electrochemical properties of LNM-0.1Ti with other Li-excess DRX cathodes reported in previous studies.[31,40−46]

associated with the (200) and (220) planes emerges at the end of the Mn^{3+}/Mn^{4+} oxidation, indicating a phase separation behavior.

This two-phase-like transition is attributed to the cooperative Jahn−Teller distortion of Mn^{3+}/Mn^{4+},[47−49] which leads to rapid contraction of Mn−O bonds. The presence of SRCO, as previously confirmed by SAED, further amplifies this distortion, accelerating the structural transformation. These changes cause spatially inhomogeneous reactions, inducing additional overpotentials and impeding oxygen redox kinetics. Consequently, the LNM suffers from low initial Coulombic efficiency and limited power capability.

During discharge, the separated (220) peaks in the LNM do not fully recover, indicating irreversible structural changes. In contrast, LNM-0.1Ti exhibits a single-phase solid-solution reaction throughout both charge and discharge processes (Figure 5b), despite undergoing the same Mn^{3+}/Mn^{4+} and O^{2-}/O^{1-} redox reactions as LNM. This indicates that Ti-substitution suppresses Jahn−Teller distortion and stabilizes the structural evolution, thus enabling improved oxygen redox activity. Ex situ XRD analysis during the initial cycle further reveals that phase separation persists in LNM even after Li reinsertion (Figure S16, Supporting Information). This difference in structural reversibility is thermodynamic in nature, induced by Ti incorporation rather than kinetics.

The initial charge profiles of the two materials reflect these structural differences. While LNM exhibits a plateau between Mn and O redox reactions, LNM-0.1Ti displays a smoother

https://doi.org/10.1021/acsnano.5c22044
ACS Nano 2026, 20, 10556−10569

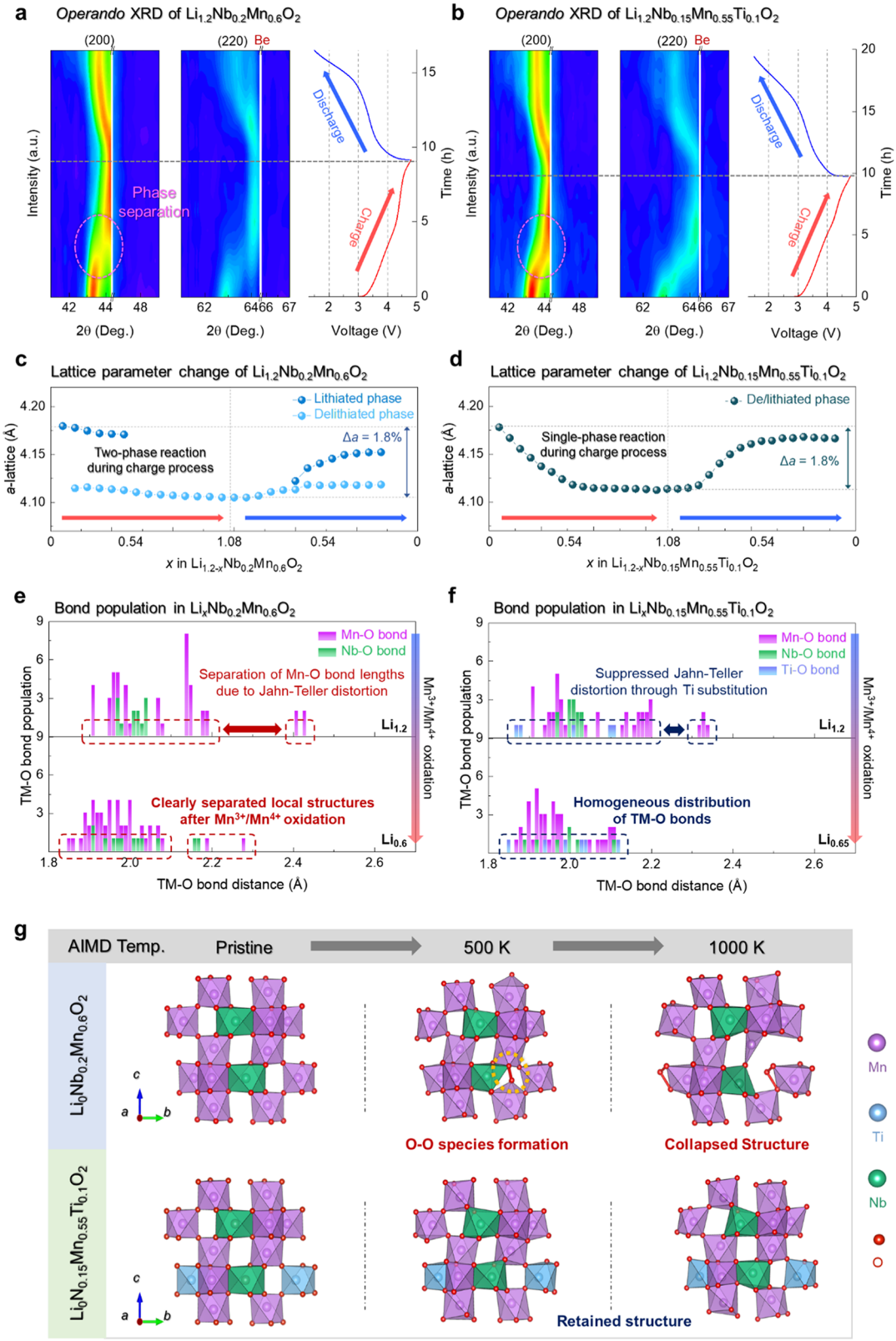

Figure 5. Comparison of *operando* XRD patterns, with a magnified view of (a) LNM and (b) LNM-0.1Ti during the initial charge/discharge in the voltage range of 1.5−4.8 V (vs Li^+/Li) at a current density of 35 mA g^{-1}. Lattice parameter changes calculated through Rietveld refinement of *operando* XRD results for (c) LNM and (d) LNM-0.1Ti. Counted TM−O bond populations in (e) Li_xNM and (f) Li_xNM-0.1Ti ($0.6 \leq x \leq 1.2$). (g) Structural stability of the modeled Li_0NM and Li_0NM-0.1Ti configurations evaluated by AIMD simulations at 500 and 1000 K, confirming the formation of O−O species due to oxidized oxygen instability in the lattice (highlighted with yellow circles). AIMD simulations were performed using the fully delithiated Li_0NM and Li_0NM-0.1Ti structures.

https://doi.org/10.1021/acsnano.5c22044
ACS Nano 2026, 20, 10556−10569

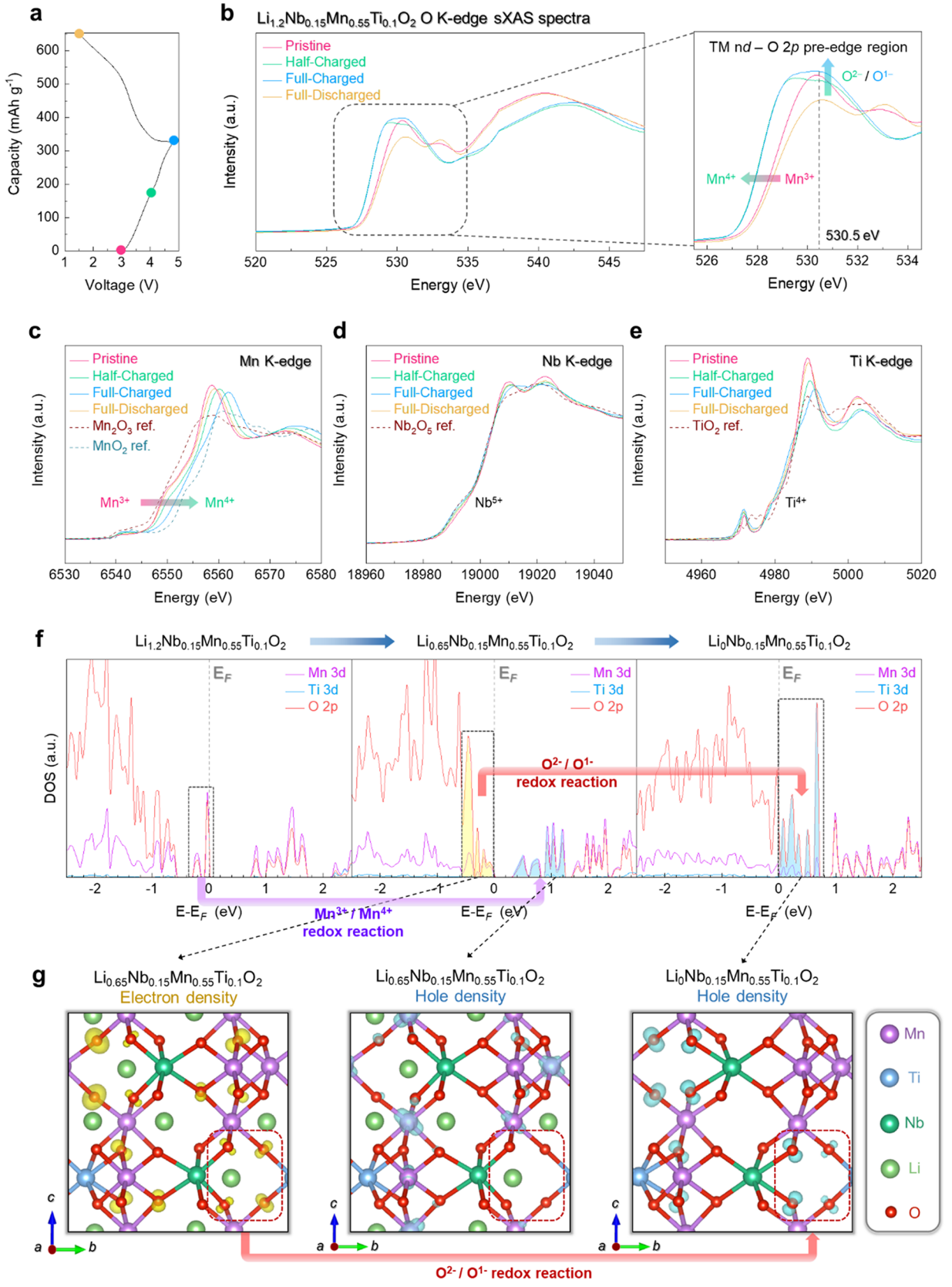

Figure 6. (a) Initial charge/discharge curves of LNM-0.1Ti with marked cutoff voltage points corresponding to ex situ analysis samples. Ex situ analysis of LNM-0.1Ti: (b) O K-edge sXAS spectra with a magnified view of the pre-edge region (right panel). (c) Mn, (d) Nb, and (e) Ti K-edge XANES spectra. (f) pDOS for Ti 3d, Mn 3d, and O 2p orbitals in Li_xNM-0.1Ti ($0 \leq x \leq 1.2$). (g) Visualized pDOS for Ti 3d, Mn 3d, and O 2p orbitals in $Li_{0.65}$NM-0.1Ti and Li_0NM-0.1Ti: electron density (yellow) and hole density (blue).

https://doi.org/10.1021/acsnano.5c22044
ACS Nano 2026, 20, 10556−10569

voltage curve (Figure 3a,b), suggesting a more homogeneous reaction pathway. Rietveld refinement of *operando* XRD data confirms that both materials exhibit a similar lattice contraction (~1.8%) during the initial charge. However, during subsequent cycles, the *a*-axis lattice parameter of LNM-0.1Ti changes by only ~0.5% compared to ~0.7% in LNM (Figure 5c,d), reflecting enhanced structural reversibility in LNM-0.1Ti. This trend is further supported by ex situ XRD after prolonged cycling, where LNM-0.1Ti retains higher peak intensities than LNM (Figure S17, Supporting Information).

DFT calculations based on stable low-energy reference configurations further support our interpretation that Jahn–Teller distortion associated with Mn^{3+} is mitigated in LNM-0.1Ti, as revealed by a comparative analysis of the Mn–O bond-length distributions. As shown in Figure 5e,f, the Mn–O bond lengths in LNM exhibit clear separation into two distinct ranges (two long bonds (≥2.4 Å) and four short bonds (≤2.2 Å)), consistent with Jahn–Teller distortion of $Mn^{3+}O_6$ octahedra. A more detailed comparison of Mn–O bond length distributions further highlights the effect of Ti-substitution. As shown in Figure 5e, the as-prepared LNM exhibits a bimodal Mn–O bond distribution, indicating strong Jahn–Teller distortion. In contrast, LNM-0.1Ti shows a narrower, more uniform distribution of Mn–O bond lengths, consistent with a reduced local distortion. These trends are in agreement with the STEM interatomic distance analysis (Figure S9, Supporting Information).

Interestingly, upon full oxidation of Mn^{4+} (i.e., in $Li_{0.6}Nb_{0.2}Mn_{0.6}O_2$), the Mn–O bonds in LNM remain significantly split, while those in $Li_{0.65}Nb_{0.15}Mn_{0.55}Ti_{0.1}O_2$ remain nearly uniform (Figure 5f). A similar trend is observed at the fully delithiated (Li_0) state after oxygen redox, with residual splitting in LNM but a largely homogeneous distribution in LNM-0.1Ti (Figure S18, Supporting Information). This suggests that even under highly oxidized conditions, the LNM-0.1Ti structure resists local lattice distortion. These findings demonstrate that disruption of SRCO mitigates abrupt local structural changes, suppresses phase separation, and thereby stabilizes the lattice during charge/discharge. This structural stabilization enables the superior electrochemical performance observed in LNM-0.1Ti.

AIMD simulations further demonstrate the structural robustness of LNM-0.1Ti. After full delithiation, $Li_0Nb_{0.2}Mn_{0.6}O_2$ shows severe lattice degradation and molecular O_2 evolution after 20 ps at 500 K. In contrast, fully Li^+-deintercalated $Li_0Nb_{0.15}Mn_{0.55}Ti_{0.1}O_2$ maintains structural integrity under the same conditions and remains stable even at 1000 K (Figure 5g). Collectively, these results demonstrate that disruption of short-range cation ordering and suppression of Mn^{3+}-induced Jahn–Teller distortion in LNM-0.1Ti enhance lattice stability during cycling, which in turn improves the reversibility of oxygen redox reactions. Moreover, the improved oxygen/lattice stability under highly oxidized conditions can also help limit sustained electrolyte oxidation at high voltage by facilitating effective early stage surface passivation, consistent with the unusually high first-cycle Coulombic efficiency observed for LNM-0.1Ti. This structural robustness underlies the superior electrochemical performance of LNM-0.1Ti, including higher energy density, improved rate capability, and prolonged cycle life.

Enhanced Oxygen Redox Activity in LNM-0.1Ti

To elucidate the redox mechanism in LNM-0.1Ti, ex situ sXAS was performed in TFY mode, providing a probing depth of ~200 nm. Electrodes were harvested in various charge/discharge states at 17.5 mA g^{-1} (Figure 6a). In the O K-edge spectra of $Li_xNb_{0.15}Mn_{0.55}Ti_{0.1}O_2$ (Li_xNM-0.1Ti) (Figure 6b), a shift of the pre-edge peak to lower energy in the half-charged state reflects increased Mn-oxidation number and hole formation on hybridized TM 3d–O 2p orbitals. At the fully charged state, an increased intensity near 530.5 eV was observed, suggesting the formation of oxidized oxygen species, indicating the activation of an anionic redox reaction.[12,50−52]

To monitor the changes in the TM valence states, we performed XANES spectroscopy. As shown in Figure 6c, the Mn K-edge shifts to higher energy during charging, confirming the oxidation of Mn^{3+} to Mn^{4+}. In contrast, negligible changes were observed in the Nb and Ti K-edges (Figure 6d,e), confirming that these d_0 ions are electrochemically inactive. These results demonstrate that charge compensation in LNM-0.1Ti proceeds via sequential Mn and O redox reactions.

To further understand the role of SRCO in tuning redox behavior, we compared the redox activity of LNM-0.1Ti with that of LNM using XAS. As shown in Figure S19 in the Supporting Information, both materials undergo sequential Mn and O redox reactions during Li^+ (de)intercalation. However, in the fully charged state, the intensity of the oxidized oxygen species (~530.5 eV) in the K-edge spectra is more pronounced in LNM-0.1Ti than in LNM (Figure S20, Supporting Information), indicating stronger participation of oxidized oxygen species. This enhanced anionic redox activity in LNM-0.1Ti is attributed to the suppression of SRCO, which likely facilitates a more homogeneous and reversible redox environment.

To support these experimental observations with theoretical investigations, DFT calculations of the pDOS were performed for Li_xNM-0.1Ti with varying Li compositions ($0 \le x \le 1.2$). As shown in Figure 6f, Mn 3d states dominate the hole densities right above the Fermi level (E_F) in $Li_{0.65}$NM-0.1Ti, confirming cationic (Mn^{3+}/Mn^{4+}) redox activity in the early stages of delithiation from $Li_{1.2}$NM-0.1Ti to $Li_{0.65}$NM-0.1Ti. On the other hand, O 2p states dominate the electron densities near E_F. In fully delithiated Li0NM-0.1Ti, significant O 2p hole states emerge above E_F, indicating that an oxygen redox reaction occurs during further Li^+ deintercalation from $Li_{0.65}$NM-0.1Ti to Li_0NM-0.1Ti, following the cationic Mn redox reaction. These features are further visualized in the electron density maps (Figure 6g), where depletion of electron density (blue) around the O atoms confirms their role in charge compensation. The corresponding pDOS and electron-density results for LNM at the same delithiation states are provided in Figure S21 in the Supporting Information for direct comparison.

To quantitatively assess the redox sequence, we also calculated the integrated spin moments of Mn and O ions in LNM-0.1Ti (Figure S22, Supporting Information). As Li is extracted from $x = 1.2$ to $x = 0.65$, the magnetic moment of Mn decreases, consistent with Mn^{3+}/Mn^{4+} oxidation. From $x = 0.65$ to $x = 0$, the Mn moment remains stable, while the O moment increases, confirming that oxygen anions participate in redox during the later stage of delithiation. Nb and Ti, as expected for d_0 ions, show negligible changes in both pDOS and magnetic moment, indicating their electrochemical inactivity.

Taken together, these results demonstrate that LNM-0.1Ti undergoes sequential cationic (Mn^{3+}/Mn^{4+}) and anionic (O^{2-}/O^-) redox reactions. The enhanced anionic redox activity is enabled by the suppression of SRCO, which creates a structurally favorable environment for oxygen redox and

https://doi.org/10.1021/acsnano.5c22044
ACS Nano 2026, 20, 10556−10569

contributes to the high energy density of LNM-0.1Ti. Based on the Mn contents, the maximum Mn^{3+}/Mn^{4+} redox capacities are ~175 mAh g^{-1} for LNM and ~165 mAh g^{-1} for LNM-0.1Ti. Given the measured first-charge capacities (312 and 327 mAh g^{-1}, respectively), the remaining capacities of ~137 mAh g^{-1} (≈44%) for LNM and ~162 mAh g^{-1} (≈50%) for LNM-0.1Ti can be attributed to anionic redox, as summarized in Tables S4 and S5 in the Supporting Information.

CONCLUSION

In this study, we demonstrated that the suppression of $[Li_3TM_3]$-type SRCO, a key factor limiting the performance of the DRX cathode, can be achieved without complex high-entropy composition by simultaneously controlling electrostatic interactions and the cationic size mismatch effect. In the Li–Nb/Mn DRX system, the incorporation of Ti^{4+}, which has a lower charge and smaller ionic radius than Nb^{5+}, promotes homogeneous Li/TM mixing and successfully hinders the formation of SRCO.

A low-entropy DRX cathode, LNM-0.1Ti exhibited effective suppression of SRCO, as confirmed by advanced electron microscopy techniques including SAED and STEM-HAADF-based FFT/inverse FFT analysis. The resulting structural modification minimizes Li-trapping and promotes the extension of Li-percolation networks, thereby facilitating more efficient Li^+ transport. As a result, low-entropy LNM-0.1Ti delivers a high reversible capacity of ~327 mAh g^{-1} and energy density of ~1026 Wh kg^{-1} at 17.5 mA g^{-1}—representing 119% and 123% of the corresponding values for LNM. This performance advantage becomes more pronounced at higher current densities, underscoring the kinetic benefits of SRCO suppression. Importantly, increasing the Ti content to 0.2 mol (LNM-0.2Ti) in the structure led to a deterioration in rate capability, despite the preservation of a DRX structure. This observation underscores that the enhanced performance of LNM-0.1Ti stems not from Ti-substitution alone but from compositional precision that optimally balances disorder and transport. Furthermore, LNM-0.1Ti exhibits superior long-term cycling stability, retaining ~71% of its initial capacity after 100 cycles compared to ~51% for LNM.

Operando XRD revealed that LNM-0.1Ti undergoes a solid-solution reaction with minimal lattice strain, while LNM exhibits a two-phase transition accompanied by large structural distortions and irreversible changes. These findings are supported by DFT calculations, which confirm that LNM-0.1Ti delivers reduced Mn^{3+}-induced Jahn–Teller distortions and enhanced thermodynamic stability under delithiated conditions compared to that of LNM. DFT and AIMD simulations further show that LNM-0.1Ti maintains uniform Mn–O bond lengths and resists structural collapse after delithiation. Theoretical investigation into the redox mechanism reveals that LNM-0.1Ti undergoes sequential Mn and O redox reactions, with stronger oxygen participation than LNM. The enhanced anionic redox activity is closely linked to the homogeneous atomic environment enabled by SRCO disruption. This structure–property relationship is further corroborated by DFT-based analysis of pDOS and magnetic moment evolution.

These findings are relevant to a broad range of DRX chemistries, offering a practical and flexible approach to designing high-energy, high-power cathodes for next-generation lithium-based batteries, including both lithium-ion and lithium-metal system.

EXPERIMENTAL SECTION

Sample Preparation

The bare $Li_{1.2}Nb_{0.2}Mn_{0.6}O_2$ (LNM), $Li_{1.2}Nb_{0.15}Mn_{0.55}Ti_{0.1}O_2$ (LNM-0.1Ti), and $Li_{1.2}Nb_{0.1}Mn_{0.5}Ti_{0.2}O_2$ (LNM-0.2Ti) were synthesized with a conventional solid-state method. Stoichiometric amounts of Li_2CO_3 (99%, Alfa Aesar), Nb_2O_5 (99.5%, Samchun), TiO_2 (99%, Samchun), and Mn_2O_3 (99.5%, Sigma-Aldrich) were used for synthesis. A total 5 g of precursors and 100 mL of ethyl alcohol anhydrous (99.9%, Duksan) were uniformly mixed using a planetary high-energy ball-milling machine (Pulverisette 6, Fritsch) at 300 rpm for 5 h. After wet ball-milling, the mixture was stirred on a hot plate at 80 °C overnight. And then, the dried powder was pelletized and calcined at 950 °C for 1 h in Ar. To enhance electronic conductivity, the resulting bare powder was ground and mixed with Super P carbon using a high-energy planetary mill at 300 rpm for 12 h.

Material Characterization

X-ray diffraction (XRD) data was collected to verify the crystal structure using Malvern PANalytical Empyrean with Mo Kα radiation (λ = 0.71 Å) in the 2θ range of 5–35° with a step size of 0.016°. Rietveld refinement of XRD results was performed to obtain detailed structure information using FullProf software.[53] *Operando* XRD data was obtained using an in situ XRD battery cell (ISBC) made by PANalytical with PDC TECH (Korea). *Operando* XRD was performed during the first charge/discharge at a current density of 35 mA g^{-1} in the voltage range of 1.5–4.8 V (vs Li^+/Li). All angles in the XRD pattern were transformed using Cu K_α radiation (λ = 1.54 Å) for easy comparison with those in previous studies.

The atomic ratio of elements, such as Li, Nb, Mn, and Ti, was determined using an inductively coupled plasma emission spectrometer (ICP-AES; OPTIMA 8300, PerkinElmer).

X-ray absorption spectroscopy (XAS) spectra were obtained at beamline 10C Nano-XAFS at the Pohang Accelerate Laboratory (PAL), South Korea. The collected data was measured in transmission mode, and reference data were simultaneously collected using Mn, Nb, and Ti metal foil. Also, O K-edge soft XAS (sXAS) spectra were obtained in total fluorescence yield (TFY) mode at beamline 4D-PES at PAL. All of the XAS data were normalized using Athena software.[54]

High-resolution transmission electron microscopy (HR-TEM) images, *d*-spacing with selected area electron diffraction (SAED) patterns, and energy-dispersive X-ray spectroscopy (EDS) mapping images were collected using field-emission transmission electron microscopy (FE-TEM: JEM-ARM300F, JEOL Ltd.). Atomic-scale scanning transmission electron microscopy high-angle annular dark-field (STEM-HAADF) imaging was performed using a JEM-ARM300F microscope equipped with a spherical aberration corrector and operated at an accelerating voltage of 300 kV. An atomic intensity mapping approach was employed to visualize the relative variation in atomic contrast and identify the spatial distribution of the Li^+ diffusion path. Intensities of individual atoms were quantified based on STEM-HAADF images. A 22 × 22 grid of atomic positions was extracted and digitally expanded to a 704 × 704 pixel to enhance the resolution.

The morphology of the prepared particles was observed by using field-emission scanning electron microscopy (FE-SEM: JSM-7600, JEOL Ltd.). A Pt coating was implemented to improve the electronic conductivity of the prepared samples.

Electrochemical Characterization

The electrodes were prepared with a final composition of 70 wt % of the actual active material, 20 wt % of Super P conductive carbon, and 10 wt % of polyvinylidene fluoride (PVdF). *N*-Methyl-2-pyrrolidone (NMP) was used as the solvent, and slurry was cast on the Al current collector (15 μm thickness). The electrodes were dried at 100 °C overnight in a vacuum oven. The active mass loading of the electrode was ~2 mg cm^{-2}. The CR-2032 type coin cell was assembled in an Ar-filled glovebox. The electrochemical performance was evaluated with a half cell composed of Li metal as a counter electrode, separator (Celgard 2400), and 1.2 M $LiPF_6$ in ethylene carbonate (EC):dimethyl carbonate (DMC):ethyl methyl carbonate (EMC) = 2:4:4 (v/v %) as

https://doi.org/10.1021/acsnano.5c22044
ACS Nano 2026, 20, 10556–10569

the electrolyte. An automatic charge/discharge system (WBCS 3000, WonATech) was used for the galvanostatic charge/discharge test. The power capability of electrodes was tested at various discharge current densities (17.5, 35, 70, 175, 350, and 700 mA g^{-1}) in the voltage range of 1.5−4.8 V (vs Li^+/Li).

Computational Details

All the density functional theory (DFT) calculations were executed using the Vienna Ab initio Simulation Package (VASP).[55] Project-augmented wave (PAW) pseudopotentials were used with a plane-wave basis set, as implemented in VASP.[56] Perdew−Burke−Ernzerhof (PBE) parametrization of the generalized gradient approximation (GGA) was used for the exchange−correlation functional.[57] For the DFT calculations, a 6 × 6 × 3 *k*-point grid was used to calculate a 2 × 3 × 1 supercell structure of disordered rocksalt-type $Li_{14}Nb_2Mn_8O_{24}$ and $Li_{13}Nb_2Ti_1Mn_7O_{24}$. The GGA + *U* method was applied to manage the localization of the d-orbital in Mn and Ti ions, with a *U* value of 3.9 and 2.4 eV, as used in a former study.[58] A kinetic energy cutoff of 500 eV was used in all the converged to within 0.03 eV $Å^{-1}$. Cluster-assisted statistical mechanics (CASM) was applied to generate all the Li^+/vacancy configurations for each composition.[59] The crystal structures of calculated configuration were drawn using VESTA software.[60]

Ab initio molecular dynamics (AIMD) simulations were carried out in the canonical (NVT) ensemble using the Nosé−Hoover thermostat, as implemented in VASP.[61,62] The PAW method was used with the PBE exchange−correlation functional. The pseudopotentials for Mn, Ti and Nb, and O were taken from the standard VASP library.[63] Simulations were performed at 500 and 1000 K for 20 ps with a time step of 4 fs.

■ ASSOCIATED CONTENT

Supporting Information

The Supporting Information is available free of charge at https://pubs.acs.org/doi/10.1021/acsnano.5c22044.

XRD patterns; SEM images; XAS spectra; schematic diagram; interatomic distance based on STEM-HAADF; electrochemical test; EIS spectra; DFT calculations; detailed structural information; and ICP-AES results (PDF)

■ AUTHOR INFORMATION

Corresponding Authors

Jihyun Hong − *Department of Battery Engineering, Graduate Institute of Ferrous & Eco Materials Technology (GIFT), Pohang University of Science and Technology, Pohang 37673, Republic of Korea;* orcid.org/0000-0001-7210-2901; Email: jhong@postech.ac.kr

Jongsoon Kim − *Department of Energy Science, Sungkyunkwan University, Suwon 16419, Republic of Korea; SKKU Institute of Energy Science and Technology (SIEST) and Department of Future Energy Engineering, Sungkyunkwan University, Suwon 16419, Republic of Korea;* orcid.org/0000-0002-7651-5516; Email: jongsoonkim@skku.edu

Authors

Jinho Ahn − *Department of Energy Science, Sungkyunkwan University, Suwon 16419, Republic of Korea; SKKU Institute of Energy Science and Technology (SIEST), Sungkyunkwan University, Suwon 16419, Republic of Korea*

Bonyoung Ku − *Department of Energy Science, Sungkyunkwan University, Suwon 16419, Republic of Korea; SKKU Institute of Energy Science and Technology (SIEST), Sungkyunkwan University, Suwon 16419, Republic of Korea*

Hyunji Kweon − *Department of Energy Science, Sungkyunkwan University, Suwon 16419, Republic of Korea; SKKU Institute of Energy Science and Technology (SIEST), Sungkyunkwan University, Suwon 16419, Republic of Korea*

Hoseok Lee − *SKKU Institute of Energy Science and Technology (SIEST) and Department of Future Energy Engineering, Sungkyunkwan University, Suwon 16419, Republic of Korea*

Hobin Ahn − *Department of Energy Science, Sungkyunkwan University, Suwon 16419, Republic of Korea*

Myungeun Choi − *Department of Energy Science, Sungkyunkwan University, Suwon 16419, Republic of Korea; SKKU Institute of Energy Science and Technology (SIEST), Sungkyunkwan University, Suwon 16419, Republic of Korea*

Myeong Hwan Lee − *Department of Energy Science, Sungkyunkwan University, Suwon 16419, Republic of Korea; Advanced Energy Materials Research Center, Korea Research Institute of Chemical Technology (KRICT), Daejeon 34114, Republic of Korea;* orcid.org/0000-0002-9583-730X

Moonsu Yoon − *School of Chemical, Biological and Battery Engineering, Gachon University, Seongnam-si, Gyeonggi-do 13120, Republic of Korea*

Junghyun Choi − *School of Chemical, Biological and Battery Engineering, Gachon University, Seongnam-si, Gyeonggi-do 13120, Republic of Korea;* orcid.org/0000-0003-4577-7967

Complete contact information is available at: https://pubs.acs.org/10.1021/acsnano.5c22044

Author Contributions

¶J. A. and B. K. contributed equally to this work.

Notes

The authors declare no competing financial interest.

■ ACKNOWLEDGMENTS

This work was supported by the National R&D Program through the National Research Foundation of Korea (NRF) funded by the Ministry of Science and ICT (RS-2024-00408156 (50%)) of Republic of Korea. Also, this work was partly supported by the Korea Institute for Advancement of Technology (KIAT) grant funded by the Korea Government (MOTIE) (RS-2024-00419413, HRD Program for Industrial Innovation) and Electronics and Telecommunications Research Institute (ETRI) (25YB2200, Development of Fundamental Technology for Non-Lithium Resources Based Next Generation Aqueous-Type Multivalence-Metal-Ion Battery). This work was also supported by the 2024 KRICT−SKKU Bilateral Research Program funded by the Korea Research Institute of Chemical Technology and Sungkyunkwan University.

■ REFERENCES

(1) Hansen, J. E.; Sato, M.; Simons, L.; Nazarenko, L. S.; Sangha, I.; Kharecha, P.; Zachos, J. C.; von Schuckmann, K.; Loeb, N. G.; Osman, M. B.; Jin, Q.; Tselioudis, G.; Jeong, E.; Lacis, A.; Ruedy, R.; Russell, G.; Cao, J.; Li, J. Global warming in the pipeline. *Oxf. Open Clim. Change* **2023**, *3* (1), kgad008.

(2) Sayed, E.; Olabi, A.; Alami, A.; Radwan, A.; Mdallal, A.; Rezk, A.; Abdelkareem, M. Renewable Energy and Energy Storage Systems. *Energies* **2023**, *16* (3), 1415.

(3) Levin, T.; Bistline, J.; Sioshansi, R.; Cole, W. J.; Kwon, J.; Burger, S. P.; Crabtree, G. W.; Jenkins, J. D.; O'Neil, R.; Korpås, M.; Wogrin, S.; Hobbs, B. F.; Rosner, R.; Srinivasan, V.; Botterud, A. Energy storage solutions to decarbonize electricity through enhanced capacity expansion modelling. *Nat. Energy* **2023**, *8* (11), 1199−1208.

(4) Suh, J. H.; Han, S. A.; Yang, S. Y.; Lee, J. W.; Shimada, Y.; Lee, S. M.; Lee, J. W.; Park, M. S.; Kim, J. H. Toward Fast-Charging and Dendritic-Free Li Growth on Natural Graphite Through Intercalation/Conversion on MoS2 Nanosheets. *Adv. Mater.* **2025**, *37* (7), 2414117.
(5) Aghmadi, A.; Mohammed, O. A. Energy Storage Systems: Technologies and High-Power Applications. *Batteries* **2024**, *10* (4), 141.
(6) Lauro, S. N.; Burrow, J. N.; Mullins, C. B. Restructuring the lithium-ion battery: A perspective on electrode architectures. *eScience* **2023**, *3* (4), 100152.
(7) Xu, P.; Tan, D. H. S.; Jiao, B.; Gao, H.; Yu, X.; Chen, Z. A Materials Perspective on Direct Recycling of Lithium-Ion Batteries: Principles, Challenges and Opportunities. *Adv. Funct. Mater.* **2023**, *33* (14), 2213168.
(8) Mun, J.; Song, T.; Park, M. S.; Kim, J. H. Paving the Way for Next-Generation All-Solid-State Batteries: Dry Electrode Technology. *Adv. Mater.* **2025**, *37* (36), No. e2506123.
(9) Suh, J. H.; Lee, H.; Kim, J.; Bae, H.; Shim, J. H.; Pang, W. K.; Kim, Y. H.; Kim, S.; Mun, J.; Song, T.; Kim, J. H. Strategic Lithium-Ion Battery Recycling for Global Resource Challenges. *Carbon Neutralization* **2025**, *4* (4), No. e70018.
(10) Park, G. T.; Park, N. Y.; Ryu, H. H.; Sun, H. H.; Hwang, J. Y.; Sun, Y. K. Nano-rods in Ni-rich layered cathodes for practical batteries. *Chem. Soc. Rev.* **2024**, *53* (23), 11462−11518.
(11) Ho, V.-C.; Huynh, T. N.; Jung, H.-G.; Kim, J. H.; Oh, S.-M.; Kim, Y.-J.; Mun, J. Dry carbon nanotube wrapping of Ni-rich layered oxide cathodes for lithium-ion batteries. *Sustainable Mater. Technol.* **2025**, *43*, No. e01287.
(12) Lee, Y.; Park, H.; Cho, M. k.; Ahn, J.; Ko, W.; Kang, J.; Choi, Y. J.; Kim, H.; Park, I.; Ryu, W. H.; Hong, J.; Kim, J. Li-Rich Mn−Mg Layered Oxide as a Novel Ni-/Co-Free Cathode. *Adv. Funct. Mater.* **2022**, *32* (36), 2204354.
(13) Kim, J.; Ahn, H.; Ahn, J.; Park, H.; Hong, J.; Hwan Lee, M.; Park, H.; Kim, J. Activation of Oxygen Redox by Inhibited Dynamic Phase Transition for High-Energy Li-Rich Layered Oxide Cathode. *Chem. Eng. J.* **2024**, *495*, 153122.
(14) Kang, S.; Choi, D.; Lee, H.; Choi, B.; Kang, Y. M. A Mechanistic Insight into the Oxygen Redox of Li-Rich Layered Cathodes and their Related Electronic/Atomic Behaviors Upon Cycling. *Adv. Mater.* **2023**, *35* (43), No. e2211965.
(15) Seo, D. H.; Lee, J.; Urban, A.; Malik, R.; Kang, S.; Ceder, G. The structural and chemical origin of the oxygen redox activity in layered and cation-disordered Li-excess cathode materials. *Nat. Chem.* **2016**, *8* (7), 692−697.
(16) Rahman, M. M.; Lin, F. Oxygen Redox Chemistry in Rechargeable Li-Ion and Na-Ion Batteries. *Matter* **2021**, *4* (2), 490−527.
(17) House, R. A.; Marie, J.-J.; Pérez-Osorio, M. A.; Rees, G. J.; Boivin, E.; Bruce, P. G. The role of O2 in O-redox cathodes for Li-ion batteries. *Nat. Energy* **2021**, *6* (8), 781−789.
(18) Eum, D.; Kim, B.; Kim, S. J.; Park, H.; Wu, J.; Cho, S. P.; Yoon, G.; Lee, M. H.; Jung, S. K.; Yang, W.; Seong, W. M.; Ku, K.; Tamwattana, O.; Park, S. K.; Hwang, I.; Kang, K. Voltage decay and redox asymmetry mitigation by reversible cation migration in lithium-rich layered oxide electrodes. *Nat. Mater.* **2020**, *19* (4), 419−427.
(19) Ahn, J.; Kang, J.; Cho, M. k.; Park, H.; Ko, W.; Lee, Y.; Kim, H. S.; Jung, Y. H.; Jeon, T. Y.; Kim, H.; Ryu, W. H.; Hong, J.; Kim, J. Selective Anionic Redox and Suppressed Structural Disordering Enabling High-Energy and Long-Life Li-Rich Layered-Oxide Cathode. *Adv. Energy Mater.* **2021**, *11* (47), 2102311.
(20) Clément, R. J.; Lun, Z.; Ceder, G. Cation-disordered rocksalt transition metal oxides and oxyfluorides for high energy lithium-ion cathodes. *Energy Environ. Sci.* **2020**, *13* (2), 345−373.
(21) Chen, R.; Ren, S.; Knapp, M.; Wang, D.; Witter, R.; Fichtner, M.; Hahn, H. Disordered Lithium-Rich Oxyfluoride as a Stable Host for Enhanced Li+ Intercalation Storage. *Adv. Energy Mater.* **2015**, *5* (9), 1401814.
(22) Lee, J.; Seo, D.-H.; Balasubramanian, M.; Twu, N.; Li, X.; Ceder, G. A new class of high capacity cation-disordered oxides for rechargeable lithium batteries: Li−Ni−Ti−Mo oxides. *Energy Environ. Sci.* **2015**, *8* (11), 3255−3265.
(23) Yabuuchi, N. Material Design Concept of Lithium-Excess Electrode Materials with Rocksalt-Related Structures for Rechargeable Non-Aqueous Batteries. *Chem. Rec.* **2019**, *19* (4), 690−707.
(24) McColl, K.; House, R. A.; Rees, G. J.; Squires, A. G.; Coles, S. W.; Bruce, P. G.; Morgan, B. J.; Islam, M. S. Transition metal migration and O(2) formation underpin voltage hysteresis in oxygen-redox disordered rocksalt cathodes. *Nat. Commun.* **2022**, *13* (1), 5275.
(25) Lee, J.; Urban, A.; Li, X.; Su, D.; Hautier, G.; Ceder, G. Unlocking the Potential of Cation-Disordered Oxides for Rechargeable Lithium Batteries. *SCIENCE* **2014**, *343* (6170), 519−522.
(26) Li, H.; Fong, R.; Woo, M.; Ahmed, H.; Seo, D.-H.; Malik, R.; Lee, J. Toward high-energy Mn-based disordered-rocksalt Li-ion cathodes. *Joule* **2022**, *6* (1), 53−91.
(27) Urban, A.; Lee, J.; Ceder, G. The Configurational Space of Rocksalt-Type Oxides for High-Capacity Lithium Battery Electrodes. *Adv. Energy Mater.* **2014**, *4* (13), 1400478.
(28) Kan, W. H.; Deng, B.; Xu, Y.; Shukla, A. K.; Bo, T.; Zhang, S.; Liu, J.; Pianetta, P.; Wang, B.-T.; Liu, Y.; Chen, G. Understanding the Effect of Local Short-Range Ordering on Lithium Diffusion in Li1.3Nb0.3Mn0.4O2 Single-Crystal Cathode. *Chem* **2018**, *4* (9), 2108−2123.
(29) Clément, R. J.; Kitchaev, D.; Lee, J.; Gerbrand, C. Short-Range Order and Unusual Modes of Nickel Redox in a Fluorine-Substituted Disordered Rocksalt Oxide Lithium-Ion Cathode. *Chem. Mater.* **2018**, *30* (19), 6945−6956.
(30) Squires, A. G.; Scanlon, D. O. Understanding the limits to short-range order suppression in many-component disordered rock salt lithium-ion cathode materials. *J. Mater. Chem. A* **2023**, *11* (25), 13765−13773.
(31) Ji, H.; Urban, A.; Kitchaev, D. A.; Kwon, D. H.; Artrith, N.; Ophus, C.; Huang, W.; Cai, Z.; Shi, T.; Kim, J. C.; Kim, H.; Ceder, G. Hidden structural and chemical order controls lithium transport in cation-disordered oxides for rechargeable batteries. *Nat. Commun.* **2019**, *10* (1), 592.
(32) Huang, L.; Zhong, P.; Ha, Y.; Cai, Z.; Byeon, Y. W.; Huang, T. Y.; Sun, Y.; Xie, F.; Hau, H. M.; Kim, H.; Balasubramanian, M.; McCloskey, B. D.; Yang, W.; Ceder, G. Optimizing Li-Excess Cation-Disordered Rocksalt Cathode Design Through Partial Li Deficiency. *Adv. Energy Mater.* **2023**, *13* (4), 2202345.
(33) Li, T.; Geraci, T. S.; Koirala, K. P.; Zohar, A.; Bassey, E. N.; Chater, P. A.; Wang, C.; Navrotsky, A.; Clement, R. J. Structural Evolution in Disordered Rock Salt Cathodes. *J. Am. Chem. Soc.* **2024**, *146* (35), 24296−24309.
(34) Wang, R.; Li, X.; Liu, L.; Lee, J.; Seo, D.-H.; Bo, S.-H.; Urban, A.; Ceder, G. A disordered rock-salt Li-excess cathode material with high capacity and substantial oxygen redox activity: Li 1.25 Nb 0.25 Mn 0.5 O 2. *Electrochem. Commun.* **2015**, *60*, 70−73.
(35) Li, L.; Ouyang, B.; Lun, Z.; Huo, H.; Chen, D.; Yue, Y.; Ophus, C.; Tong, W.; Chen, G.; Ceder, G.; Wang, C. Atomic-scale probing of short-range order and its impact on electrochemical properties in cation-disordered oxide cathodes. *Nat. Commun.* **2023**, *14* (1), 7448.
(36) Hata, S.; Matsumura, S.; Kuwano, N.; Oki, K. Short range order and its transformation to long range order in Ni4Mo. *Acta Mater.* **1998**, *46* (3), 881−892.
(37) Mitome, M.; Kohiki, S.; Murakawa, Y.; Hori, K.; Kurashima, K.; Bando, Y. Transmission electron microscopy and electron diffraction study of the short-range ordering structure of alpha-LiFeO2. *Acta Crystallogr. B* **2004**, *60* (6), 698−704.
(38) Cai, Z.; Zhang, Y. Q.; Lun, Z.; Ouyang, B.; Gallington, L. C.; Sun, Y.; Hau, H. M.; Chen, Y.; Scott, M. C.; Ceder, G. Thermodynamically Driven Synthetic Optimization for Cation-Disordered Rock Salt Cathodes. *Adv. Energy Mater.* **2022**, *12* (21), 2103923.
(39) Holstun, T.; Mishra, T. P.; Huang, L.; Hau, H. M.; Anand, S.; Yang, X.; Ophus, C.; Bustillo, K.; Ma, L.; Ehrlich, S.; Ceder, G. Accelerating the Electrochemical Formation of the delta Phase in Manganese-Rich Rocksalt Cathodes. *Adv. Mater.* **2025**, *37* (6), No. e2412871.

https://doi.org/10.1021/acsnano.5c22044
ACS Nano 2026, 20, 10556−10569

(40) Yabuuchi, N.; Nakayama, M.; Takeuchi, M.; Komaba, S.; Hashimoto, Y.; Mukai, T.; Shiiba, H.; Sato, K.; Kobayashi, Y.; Nakao, A.; Yonemura, M.; Yamanaka, K.; Mitsuhara, K.; Ohta, T. Origin of stabilization and destabilization in solid-state redox reaction of oxide ions for lithium-ion batteries. *Nat. Commun.* **2016**, *7*, 13814.
(41) Lee, J.; Papp, J. K.; Clement, R. J.; Sallis, S.; Kwon, D. H.; Shi, T.; Yang, W.; McCloskey, B. D.; Ceder, G. Mitigating oxygen loss to improve the cycling performance of high capacity cation-disordered cathode materials. *Nat. Commun.* **2017**, *8* (1), 981.
(42) Kwon, D.-H.; Lee, J.; Artrith, N.; Kim, H.; Wu, L.; Lun, Z.; Tian, Y.; Zhu, Y.; Ceder, G. The Impact of Surface Structure Transformations on the Performance of Li-Excess Cation-Disordered Rocksalt Cathodes. *Cell Rep. Phys. Sci.* **2020**, *1* (9), 100187.
(43) Yu, Z.; Qu, X.; Dou, A.; Su, M.; Liu, Y.; Wu, F. Synthesis and Redox Mechanism of Cation-Disordered, Rock-Salt Cathode-Material Li-Ni-Ti-Nb-O Compounds for a Li-Ion Battery. *ACS Appl. Mater. Interfaces* **2019**, *11* (39), 35777−35787.
(44) Fong, R.; Mubarak, N.; Park, S. W.; Lazaris, G.; Liu, Y.; Malik, R.; Seo, D. H.; Lee, J. Redox Engineering of Fe-Rich Disordered Rock-Salt Li-Ion Cathode Materials. *Adv. Energy Mater.* **2024**, *14* (22), 2400402.
(45) Huang, J.; Zhong, P.; Ha, Y.; Kwon, D.-H.; Crafton, M. J.; Tian, Y.; Balasubramanian, M.; McCloskey, B. D.; Yang, W.; Ceder, G. Non-topotactic reactions enable high rate capability in Li-rich cathode materials. *Nat. Energy* **2021**, *6* (7), 706−714.
(46) Kan, W. H.; Wei, C.; Chen, D.; Bo, T.; Wang, B. T.; Zhang, Y.; Tian, Y.; Lee, J. S.; Liu, Y.; Chen, G. Evolution of Local Structural Ordering and Chemical Distribution upon Delithiation of a Rock Salt−Structured Li1.3Ta0.3Mn0.4O2 Cathode. *Adv. Funct. Mater.* **2019**, *29* (17), 1808294.
(47) Lun, Z.; Ouyang, B.; Kwon, D. H.; Ha, Y.; Foley, E. E.; Huang, T. Y.; Cai, Z.; Kim, H.; Balasubramanian, M.; Sun, Y.; Huang, J.; Tian, Y.; Kim, H.; McCloskey, B. D.; Yang, W.; Clement, R. J.; Ji, H.; Ceder, G. Cation-disordered rocksalt-type high-entropy cathodes for Li-ion batteries. *Nat. Mater.* **2021**, *20* (2), 214−221.
(48) Ceder, G. First-principles alloy theory in oxides. *Modell. Simul. Mater. Sci. Eng.* **2000**, *8*, 311−321.
(49) Radin, M. D.; Hy, S.; Sina, M.; Fang, C.; Liu, H.; Vinckeviciute, J.; Zhang, M.; Whittingham, M. S.; Meng, Y. S.; Van der Ven, A. Narrowing the Gap between Theoretical and Practical Capacities in Li-Ion Layered Oxide Cathode Materials. *Adv. Energy Mater.* **2017**, *7* (20), 1602888.
(50) Gent, W. E.; Lim, K.; Liang, Y.; Li, Q.; Barnes, T.; Ahn, S. J.; Stone, K. H.; McIntire, M.; Hong, J.; Song, J. H.; Li, Y.; Mehta, A.; Ermon, S.; Tyliszczak, T.; Kilcoyne, D.; Vine, D.; Park, J. H.; Doo, S. K.; Toney, M. F.; Yang, W.; Prendergast, D.; Chueh, W. C. Coupling between oxygen redox and cation migration explains unusual electrochemistry in lithium-rich layered oxides. *Nat. Commun.* **2017**, *8* (1), 2091.
(51) Lin, F.; Nordlund, D.; Markus, I. M.; Weng, T.-C.; Xin, H. L.; Doeff, M. M. Profiling the nanoscale gradient in stoichiometric layered cathode particles for lithium-ion batteries. *Energy Environ. Sci.* **2014**, *7* (9), 3077.
(52) Kim, J.; Pang, W. K.; Mun, J.; Song, T.; Chen, J.; Kim, J. H.; Yoon, D. H. Prospect of Ruthenium for Hydrogen Evolution Reaction in Alkaline Media through In Situ Monitoring. *Adv. Energy Mater.* **2025**, *15* (33), 2502858.
(53) Rodríguez-Carvajal, J. Recent developments of the program FULLPROF, commission on powder diffraction. *IUCr. Newsl.* **2001**, *26*, 12−19.
(54) Ravel, B.; Newville, M. ATHENA and ARTEMIS: Interactive Graphical Data Analysis Using IFEFFIT. *Phys. Scr., T* **2005**, *T115*, 1007−1010.
(55) Kresse, G.; Furthmüller, J. Efficiency of Ab-Initio Total Energy Calculations for Metals and Semiconductors Using a Plane-Wave Basis Set. *Comput. Mater. Sci.* **1996**, *6* (1), 15−50.
(56) Blöchl, P. E. Projector Augmented-Wave Method. *Phys. Rev. B:Condens. Matter Mater. Phys.* **1994**, *50* (24), 17953−17979.
(57) Perdew, J. P.; Burke, K.; Ernzerhof, M. Generalized Gradient Approximation Made Simple. *Phys. Rev. Lett.* **1996**, *77* (18), 3865−3868.
(58) Seo, D. H.; Lee, J.; Urban, A.; Malik, R.; Kang, S.; Ceder, G. The Structural and Chemical Origin of the Oxygen Redox Activity in Layered and Cation-Disordered Li-Excess Cathode Materials. *Nat. Chem.* **2016**, *8* (7), 692−697.
(59) Van der Ven, A.; Thomas, J. C.; Xu, Q.; Bhattacharya, J. Linking the Electronic Structure of Solids to Their Thermodynamic and Kinetic Properties. *Math. Comput. Simul.* **2010**, *80* (7), 1393−1410.
(60) Momma, K.; Izumi, F. VESTA: A Three-Dimensional Visualization System. *J. Appl. Crystallogr.* **2008**, *41*, 653.
(61) Ramos, E. P.; Zhang, Z.; Assoud, A.; Kaup, K.; Lalère, F.; Nazar, L. F. Correlating Ion Mobility and Single Crystal Structure in Sodium-Ion Chalcogenide-Based Solid State Fast Ion Conductors: Na 11 Sn 2 PnS 12 (Pn = Sb, P). *Chem. Mater.* **2018**, *30* (21), 7413−7417.
(62) Zhang, Z.; Roy, P.-N.; Li, H.; Avdeev, M.; Nazar, L. F. Coupled Cation−Anion Dynamics Enhances Cation Mobility in Room-Temperature Superionic Solid-State Electrolytes. *J. Am. Chem. Soc.* **2019**, *141* (49), 19360−19372.
(63) Kresse, G.; Joubert, D. From Ultrasoft Pseudopotentials to the Projector Augmented-Wave Method. *Phys. Rev. B:Condens. Matter Mater. Phys.* **1999**, *59* (3), 1758−1775.

https://doi.org/10.1021/acsnano.5c22044
ACS Nano 2026, 20, 10556−10569